
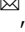



Aquifer conditions, not irradiance determine the potential of photovoltaic energy for groundwater pumping across Africa

Simon Meunier ^{1,2}, Peter K. Kitanidis³, Amaury Cordier^{1,2} & Alan M. MacDonald ⁴

Groundwater pumping using photovoltaic energy has the potential to transform water services in poorly served areas. Here we develop a numerical model that uses openly available data to simulate the abstraction capacities of photovoltaic water pumping systems across Africa. The first contribution of this article is the detailed design of the large-scale model to include realistic geological constraints on the depth of pumping and sub-hourly irradiance time series. The second one is the provision of results for the whole continent. We simulated results for three system sizes (100, 1000, 3000 W_p) and the daily pumped volumes were found to vary between 0.1 and 180 m³, depending on the size and location. We show that, for much of Africa, groundwater pumping using photovoltaic energy is constrained by aquifer conditions, rather than irradiance. Our results can help identify regions where photovoltaic pumping has the highest potential and help target large scale investments.

¹ Université Paris-Saclay, CentraleSupélec, CNRS, GeePs, 91192 Gif-sur-Yvette, France. ² Sorbonne Université, CNRS, GeePs, 75252 Paris, France.

³ Department of Civil and Environmental Engineering, Stanford University, Stanford, CA, USA. ⁴ British Geological Survey, The Lyell Centre, Research Avenue South, Edinburgh EH14 4AS Scotland, United Kingdom. ✉email: simon.meunier@centralesupelec.fr

In Africa, >300 million people use unimproved water sources for domestic use, mostly in rural off-grid areas¹. Irrigation is also limited and there are calls to increase irrigation to improve food security given increased climate variability^{2,3}. Groundwater and surface water are the main water sources. Even though surface water is often shallower and cheaper to extract, groundwater constitutes the largest and most widely distributed store of freshwater in Africa⁴ and, unlike surface water, often does not require treatment⁵. Groundwater is also suitable for irrigation because it responds more slowly to meteorological conditions and thus provides a natural buffer against climate variability^{6,7}. Currently, most rural groundwater pumping in Africa is undertaken by community handpumps^{8,9}, which have proved easily repaired and resilient to drought^{10,11}. However ongoing functionality rates can be low due to installation and maintenance issues¹². The Sustainable Development Goals call for a higher level of service, with safe water available reliably at individual households¹³. There is therefore a considerable challenge to move service levels beyond community handpumps.

Pumping systems powered by photovoltaic energy are a promising solution to improve water access in many off-grid areas without importantly increasing greenhouse gas emissions. They are already economically competitive in many contexts¹⁴, technological advances have improved their longevity¹⁵ and local case studies (e.g.,^{16–18}) have shown promising results. However, these results may not be encountered in other locations due to management issues^{4,19} and the spatial variability of groundwater and solar resources.

Some studies have investigated the potential of photovoltaic water pumping systems (PVWPS) over continuous geographical areas. These studies have been conducted in Ethiopia²⁰, Ghana²¹, Egypt^{22,23}, Algeria²⁴, Spain and Morocco²⁵, China^{26,27} and for locations with shallow groundwater (static water depth <50 m) in sub-Saharan Africa²⁸. However, articles^{20–24,26} do not use a technical model of PVWPS, which prevents consideration of the relative importance of groundwater and solar resources. The other studies^{25,27,28} consider a technical PVWPS model. Nevertheless, they use monthly average irradiance values instead of hourly/sub-hourly time series, which influences PVWPS

operation and performances^{18,29}. Additionally, they do not account for the saturated thickness of the aquifer, which restricts the maximum possible drawdown and thus pumped flow rate. Finally, existing studies do not provide results for the whole African continent, which limits comparison between different countries and regions.

Here we propose a model that uses openly available groundwater and irradiance data to simulate the abstraction capacities of PVWPS across Africa. The first contribution of this work is the detailed design of the large-scale PVWPS model to include realistic geological constraints on the depth of pumping, through the aquifer saturated thickness notably, and sub-hourly irradiance time series. Considering, for each pixel, sub-hourly irradiance time series instead of monthly average irradiance values has several advantages. First, the pumped flow rate varies non-linearly with irradiance, therefore, results from sub-hourly irradiance data are different from using averages. Secondly, in numerous cases, for high irradiance values (e.g., in the middle of the day) pumping will cease due to high drawdowns reaching the motor-pump, thus reducing the total pumped volume. This would not be observed if monthly average irradiance values were used. This is where the other specificity of the model, which consists in including a realistic geological constraint on the depth of pumping, also plays an important role. Finally, considering sub-hourly irradiance time series enables simulations for critical days of the year (notably very low irradiance days) for which the pumped volume may be very low, which can impact smooth water consumption. The second contribution of this work is the provision of results for the whole continent, including for North Africa and for locations where groundwater is deeper than 50 m, where PVWPS have particular relevance as groundwater is very difficult to access through handpumps⁴. The results are provided for three PVWPS sizes, for the whole year as well as for extreme periods of the year (e.g., low irradiance consecutive days) and compared with groundwater recharge. Providing results for the whole continent allows comparing regions between themselves and identifying regions where PVWPS have the highest potential and thus help target investments. Our results notably reveal that for 27% of the locations the largest considered system does not yield the highest volume because of too important drawdowns which reach the motor-pump thus forcing the system to stop. They also show that the main determinant of the spatial variations of the pumped volume is the aquifer conditions rather than the irradiance.

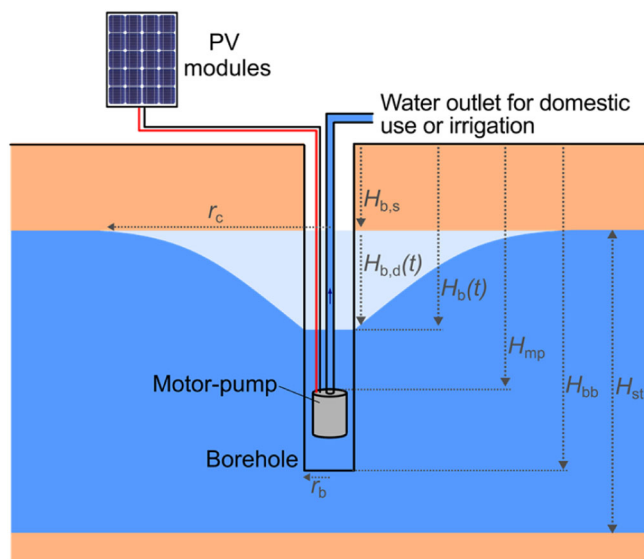


Fig. 1 Considered PVWPS architecture. All the lengths are defined as positive. r_b : borehole radius, H_{bb} : borehole depth, H_{mp} : motor-pump depth, H_{st} : aquifer saturated thickness, $H_{b,s}$: static water depth (depth when there is no pumping), $H_{b,d}$: drawdown, H_b : water depth in the borehole, r_c : radius of the cone of depression.

System, input data and model overview. The considered PVWPS architecture is shown in Fig. 1 and its operation is presented in the methods section. This architecture is common for groundwater abstraction with photovoltaic energy^{16,30}. In this article, we consider a generic PVWPS and with the size of the motor-pump proportional to the peak power of the photovoltaic (PV) modules. The peak power of the PV modules is therefore used as a proxy for the size of the PVWPS.

The characteristics of the irradiance and groundwater resources input data considered in this study are presented in Table 1. Information about the processing carried out on input data are given in the methods section. In Fig. 2, we plot the average over the year of the global horizontal irradiance G_{gh} for 2020, static water depth $H_{b,s}$, aquifer transmissivity T , saturated thickness H_{st} and groundwater recharge R .

The proposed model allows to simulate, for each location of Africa, the average daily pumped volume V by a PVWPS of peak power P_p . The block diagram of the model is presented in Supplementary Fig. 1. To compute the model results, two types of elements are required. The first one is the design parameters, which are listed in Table 2. They are set by the designer

Table 1 Original input location-dependent data.

| Data | Symbol | Description | Unit | Spatial resolution | Temporal resolution and coverage | Year of release | Provider |
|-------------------------------|-----------|---|----------------|------------------------|---|-----------------|-----------------------------------|
| Beam normal irradiance | G_{bn} | Share of the radiation which is received from the direction of the sun by a plane facing the sun. | $W\ m^{-2}$ | 0.2° ~22 km | One temporal vector for each location. Data from 2005 to 2020 with a time step of 15 min (some datapoints are missing for years 2005 to 2012). | 2021 | European Commission ⁴⁶ |
| Global horizontal irradiance | G_{gh} | Radiation received by a horizontal plane from all directions. | | | | | |
| Diffuse horizontal irradiance | G_{dh} | Share of the radiation which is received on a horizontal plane from all directions except that of the sun. | | | | | |
| Static water depth | $H_{b,s}$ | Depth of water in the borehole when there is no pumping. | m | 0.05° ~6 km | Dependence in time not provided. | 2012 | British Geological Survey |
| Aquifer transmissivity | T | Rate at which groundwater flows horizontally through an aquifer | $m^2\ s^{-1}$ | | One range of variation for each location. | | et al. ^{4,45,64-67} |
| Aquifer saturated thickness | H_{st} | Vertical thickness of the hydrogeologically defined aquifer unit in which the pore spaces are saturated with water. | m | 0.01° ~1 km | | | |
| Groundwater recharge | R | Rate at which an aquifer is replenished. | $m\ year^{-1}$ | 0.28° ~31 km | Dependence in time not provided. One value for each location. | 2020 | |

The aquifer transmissivity data T are obtained from the aquifer productivity data⁴ and the look-up table between productivity and transmissivity⁴⁵. We assume the same value of transmissivity both for fully and partially penetrating boreholes.

depending on the components chosen for the PVWPS. For the rest of the article, we choose the values presented in Table 2 for the design parameters. The second one is the location-dependent data (in particular irradiance and groundwater resources input data). Except for the albedo of the surrounding environment κ , the data are provided by the references of Table 1. We discuss about the choice of κ in the methods section. The proposed model is composed of several sub-models (see Supplementary Fig. 1). The atmospheric sub-model computes the irradiance on the plane of the PV modules G_{pv} from input irradiance data. The PV modules sub-model computes the power produced by the PV modules P from G_{pv} and the peak power of the PV modules P_p . The motor-pump sub-model computes the pumped flow rate Q from P and the total dynamic head that the motor-pump has to overcome TDH . The hydraulic sub-model computes TDH from Q , accounting for the response of the water level in the borehole to pumping and for pipe losses. The pumped flow rate Q is integrated over time to obtain the average daily pumped volume V . These sub-models are detailed in the methods section. In Fig. 3, we present the average over the year of the irradiance on optimally tilted PV modules across Africa, which is an intermediary result of the model and which is relevant for the analysis of the final results.

Results

Detailed pumped volume results for a single location. We start by detailing the model results for one given location (GPS: latitude = 6.2° , longitude = -5.2°), which is in the Ivory Coast. In Fig. 4, we plot the evolution of the pumped flow rate Q and of the water depth in the borehole H_b for three sizes of systems ($100\ W_p$, $1000\ W_p$ and $3000\ W_p$) and for this location. $100\ W_p$ corresponds to the smallest considered size of PVWPS. Indeed, the majority of PVWPS for groundwater abstraction are larger than $100\ W_p$ ^{14,31,32}. As a general order of magnitude, $1000\ W_p$ is a typical PVWPS size for domestic water access^{14,31} and $3000\ W_p$ is a

typical size for irrigation^{14,32} (the size may of course vary depending on the considered specific system). Logically, we observe that the pumped flow rate Q and thus the borehole water depth H_b follow the evolution of the irradiance. In Fig. 4c, we observe the shutdown of the motor-pump ($Q = 0$) for a long part of the day, when the borehole water depth H_b would have reached the position of the motor-pump H_{mp} (see 'PVWPS operation' in the methods section). This leads to a decrease of the pumped volume V . For instance, in this case, the average daily pumped volume V for a $1000\ W_p$ PVWPS is $15.9\ m^3$ and only $5.2\ m^3$ for a $3000\ W_p$ system.

Pumped volume maps for the whole Africa. The results for all of Africa are shown in Fig. 5 presenting the average daily pumped volume V for PVWPS of 100, 1000 and $3000\ W_p$. Results indicate that the pumped volume values vary importantly from one area to another. These values have to be compared to the water requirements for domestic use and irrigation. For domestic use, daily water requirements are ~15 L/person/day for basic access³³. Consequently, a PVWPS which extracts $5\ m^3$ per day meets the basic water needs of a village of ~330 inhabitants, although if water was available on premises individual use would rise considerably³⁴. Regarding agriculture, as a general order of magnitude, farmer led or community irrigation would typically require low yields (10 – $100\ m^3$ per day) and commercial irrigation would require larger yields, often $>200\ m^3$ per day^{4,35} (these numbers of course vary depending on the irrigated area and the crop type).

As highlighted by the detailed results on the single location, the pumped volume maps (Fig. 5) also indicate that, in certain areas (e.g., for a large portion of Zimbabwe), smaller PVWPS have greater pumping capacities than larger systems. This is notably the case where the transmissivity T and the saturated thickness H_{st} are low, and thus where an increased drawdown may reach the motor-pump depth for high irradiance levels during the day.

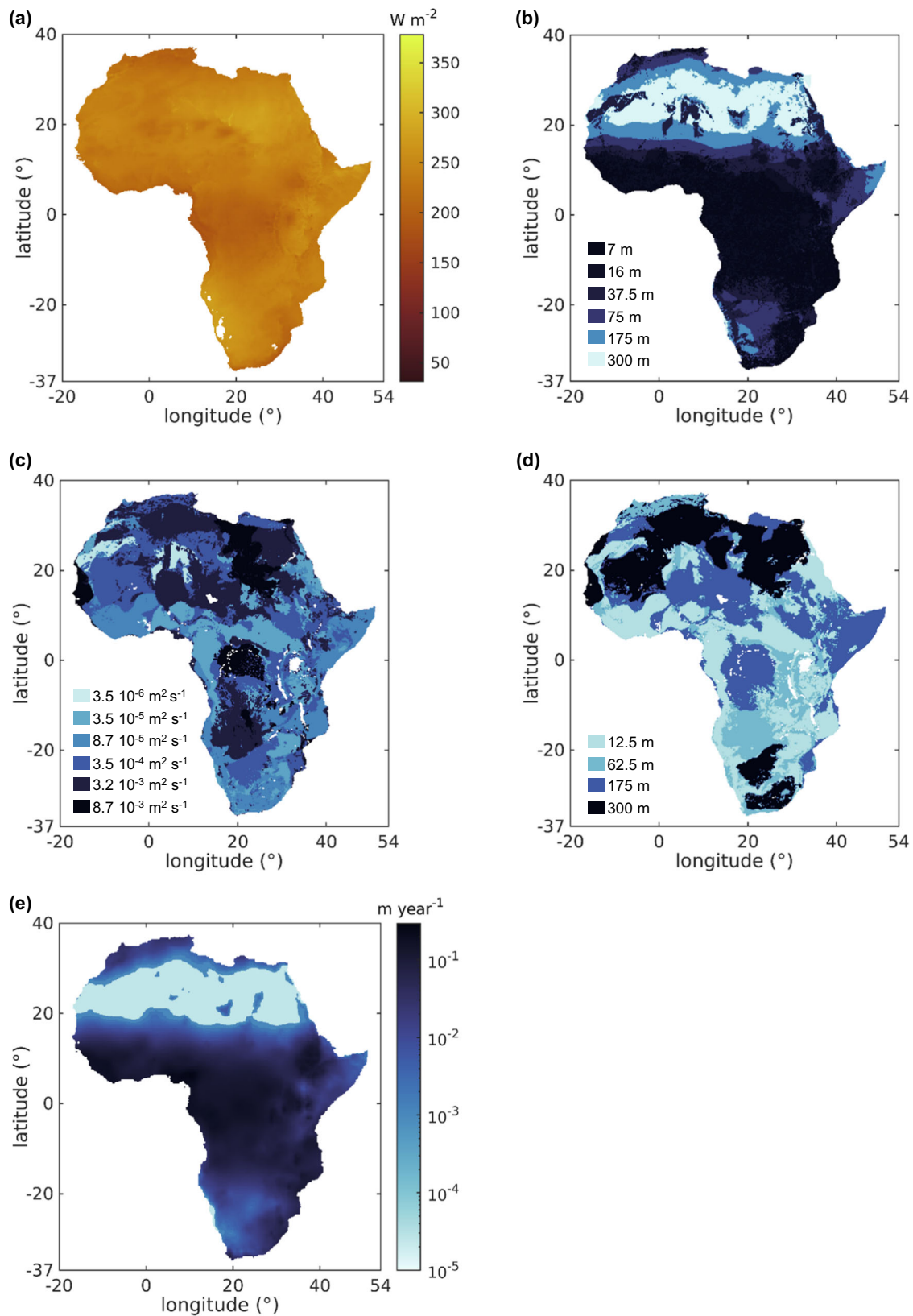


Fig. 2 Representation of selected input data. **a** global horizontal irradiance G_{gh} (average over the year for 2020, yellow scale), **b** static water depth $H_{b,s}$ (blue scale), **c** aquifer transmissivity T (blue scale), **d** aquifer saturated thickness H_{st} (blue scale), **e** groundwater recharge R (blue scale). Data sources are shown in Table 1.

Table 2 Values considered for the design parameters.

| Design parameter | Symbol | Value considered |
|---|-------------------|---|
| Azimuth of the PV modules (°) | α | Function of the latitude - see Eq. (2) in methods |
| Tilt of the PV modules (°) | θ | Function of the latitude - see Eq. (3) in methods |
| PV modules loss coefficient (-) | $C_{pv,loss}$ | 0.2 ⁵² |
| Motor-pump efficiency (-) | η_{mp} | 0.35 ⁶⁸ |
| Starting power of the motor-pump (W) | $P_{mp,0}$ | 30 W ^{68,69} |
| Minimum shut-down time of the motor-pump before attempting to restart (min) | Δt_{shut} | 30 min ⁴⁴ |
| Borehole radius (m) | r_b | 0.1 m ⁷⁰ |
| Borehole losses coefficient ($s^2 m^{-5}$) | β | $5 \times 10^4 s^2 m^{-5}$ ^{29,56} |
| Motor-pump depth (m) | H_{mp} | The motor-pump is positioned 10 m above the bottom of the borehole ⁷¹ . This puts the motor-pump as low as possible to minimize the risk of frequent stops of the motor-pump due to the drawdown reaching the motor-pump, while leaving a margin for preventing the sand at the bottom of the borehole from entering the motor-pump. |
| Borehole depth (m) | H_{bb} | If the saturated thickness is equal to 12.5 m, the borehole depth is set to $H_{b,s} + H_{st} + 10$ m and the motor-pump is thus at the bottom of the saturated thickness in this case. For saturated thicknesses larger or equal to 62.5 m, the borehole depth is set to $H_{b,s} + 60$ m. This allows to importantly intersect the saturated thickness while preventing too large borehole drilling costs ⁷² . |
| Linear pipe losses coefficient ($s^2 m^{-6}$) | ν | $8.9 \times 10^2 s^2 m^{-6}$ obtained by considering a pipe of diameter D_p of 0.052 m ⁵⁸ and of roughness ϵ of $1.5 \times 10^{-6} m$ ⁵⁸ (see methods). |
| Junction losses coefficient ($s^2 m^{-5}$) | K | $1.7 \times 10^4 s^2 m^{-5}$ which corresponds to one 90° regular threaded elbow for a pipe of diameter D_p of 0.052 m ⁵⁸ . |

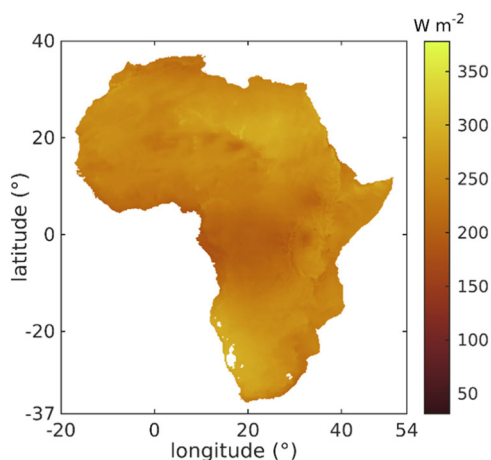


Fig. 3 Irradiance G_{pv} on optimally tilted PV modules. Average over the year for 2020 (yellow scale).

In order to better illustrate this, we present in Fig. 6a, for each pixel, the size of the system (amongst the three considered sizes) which yields the highest pumped volume V . In Fig. 6b, we show the pumped volume associated to the most effective size. We observe that, even though for the majority of cases (73%) the system of 3000 W_p extracts the highest volume, there are still a large number of cases where the systems of 100 W_p and 1000 W_p extract the most water (13 and 14% respectively).

Influence of temporal irradiance variations. In addition to the spatial variation of irradiance (highlighted for instance by Fig. 3), temporal irradiance variations also occur, which may have an impact on the pumped volume. In order to investigate the influence of inter-annual variation of irradiance, we first computed and plotted the average yearly irradiance G_{pv} and the associated pumped volume V for 2014 and 2017 for a 1000 W_p system (see Supplementary Fig. 2). We observe that the results for 2014, 2017 and 2020 are similar both in terms of average yearly

irradiance and pumped volume. When we compute, for each pixel, the difference in absolute value between the 2014 results and the 2020 results and we average the difference over Africa, we obtain differences of 2.5 % for the irradiance and 2.7 % for the pumped volume. When we compare 2017 results to 2020 results, differences of 2.5% for the irradiance and 2.8% for the pumped volume are obtained.

We then studied the influence of the variation of irradiance during the year (intra-annual variations) for 2020. First, for each pixel, we computed the monthly average irradiance for each month; and then applied the PVWPS model for a 1000 W_p system, to compute the pumped volume, using the time series of the month with the highest (Supplementary Fig. 3a, b) and lowest (Supplementary Fig. 3c, d) average irradiance. Then, we repeated for consecutive three days periods with highest (Supplementary Fig. 3e, f) and lowest (Supplementary Fig. 3g, h) average irradiance. We considered periods of three days because typically water storage systems for domestic water access are sized to hold for several low pumping days^{36,37}. Supplementary Fig. 3 reveals that, while some influence is noticed for the most and least irradiated month, the most important impact occurs for the most and least irradiated three days period. The differences in absolute value (averaged over Africa) on the pumped volume in comparison to the results for the whole 2020 (see Fig. 5b) are 16.2% and 19.7% for the best and worst month respectively; and 29.7% and 53.6% for the best and worst 3 days period respectively. This highlights the importance of considering extreme periods days when investigating the variation of the system performance over the year and its ability to enable smooth water consumption and when sizing the storage component (when it is present). For systems not limited by the drawdown reaching the motor-pump, the period with the lowest average irradiance is going to be relevant and oppositely for the other systems.

Parametric analysis and drivers of the pumped volume spatial variations. In addition to spatial and temporal irradiance variations, the values of input groundwater parameters and design parameters may also vary, which may then influence the pumped

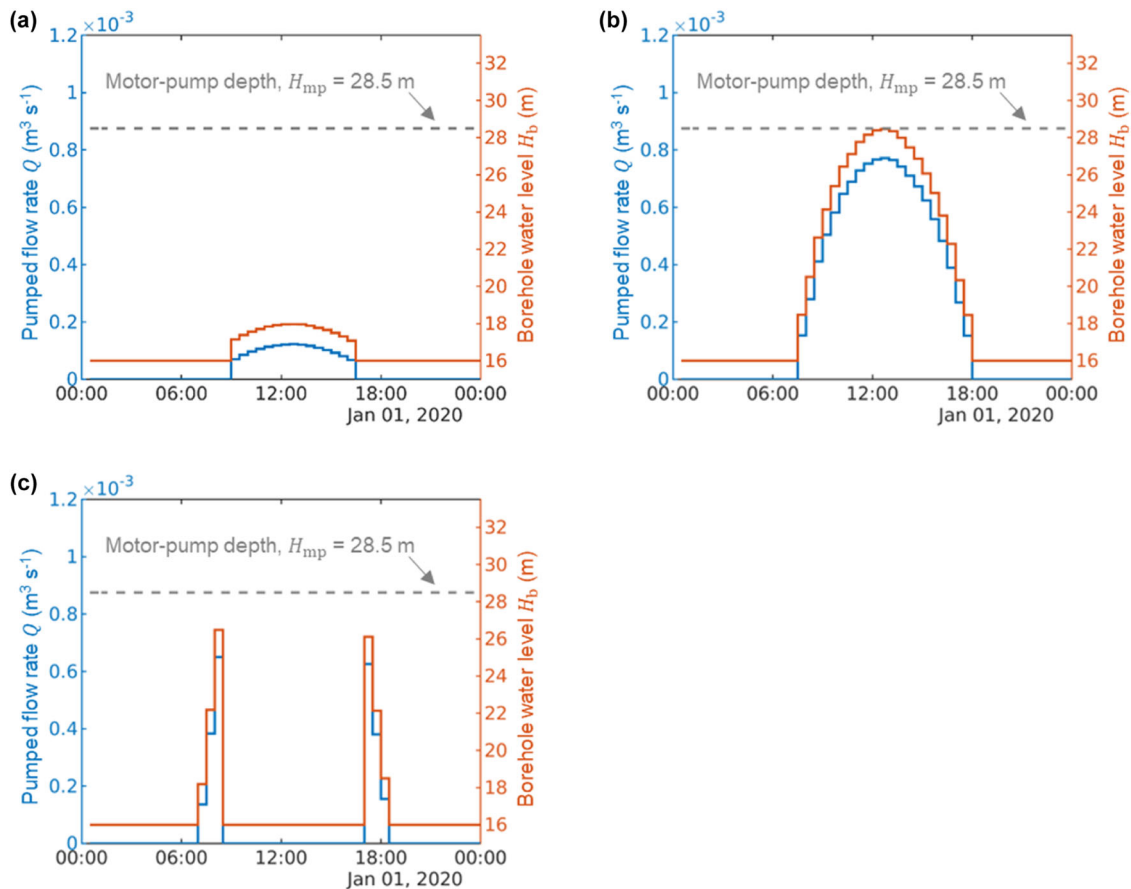


Fig. 4 Evolution of the pumped flow rate and of the borehole water depth, at the location 6.2° (lat) & -5.2° (lon), for three PVWPS sizes. **a** $P_p = 100 W_p$, **b** $P_p = 1000 W_p$, **c** $P_p = 3000 W_p$. The pumped flow rate is plotted in solid blue, the borehole water level in solid orange and the motor-pump depth with a dashed gray line.

volume V . The variation of input groundwater parameters may be due to the uncertainty in these parameters, or using local data rather than spatially averaged data. The variation of design parameters would be due to design choices. In order to investigate how a variation of input groundwater parameters and design parameters will affect the pumped volume, we consider a variation of $\pm 15\%$ and $\pm 30\%$ of input groundwater parameters and of the relevant design parameters. For each new value of the parameter, we apply the PVWPS model for 2020 for the three considered PVWPS sizes (100, 1000 and 3000 W_p) and for 100 random locations ($3 \times 100 = 300$ cases considered in total). We then compare the average pumped volume for these 300 cases to the average pumped volume for these same cases with all the parameters being at their nominal value. The results are provided in Supplementary Fig. 4a. We observe that the most influential parameters are the static water depth $H_{b,s}$ and the motor-pump efficiency η_{mp} . The transmissivity T , the saturated thickness H_{st} and the PV modules loss coefficient $c_{pv,loss}$ also have a notable influence. Considering only locations where the largest system does not yield the highest pumped volume, we observe that the transmissivity T and the saturated thickness H_{st} have the highest influence on the pumped volume (see Supplementary Fig. 4b). Indeed, for these locations, the pumped volume is strongly affected by the drawdown (which is driven by T) reaching the motor-pump position (which is set depending on H_{st}). This is also coherent with the visual inspection of the African wide maps where we see that area where the largest system does not yield the highest volume correspond to low transmissivity T and/or low saturated thickness H_{st} areas. For locations where the largest

system yields the highest volume, we observe that the static water depth $H_{b,s}$ and the motor-pump efficiency η_{mp} (which has the same influence as the irradiance $G_{pv}(t)$ on the pumped flow rate $Q(t)$, see Eq. 14 and Eq. 4) have the highest impact on the pumped volume (see Supplementary Fig. 4c). Variations in water depth $H_{b,s}$ dominate the African wide pumped volume maps for this type of locations since the spatial variability of the static water depth (between 7 and 300 m) is much higher than the one of the irradiance (average over the year between 169 and 329 $W m^{-2}$).

Comparison of pumping performances to recharge. To provide an initial estimate of the sustainability of pumping in comparison to the groundwater recharge, in Fig. 7, we plot, for each location, the ratio between the volume pumped by 50 PVWPS of most efficient capacity for 2020 (see Fig. 6) and 25% of the yearly volume recharged in a square of 22 km \times 22 km. The yearly volume recharged is computed by multiplying the recharge R in the pixel (in m/year) by the area of the square (22 km \times 22 km). We choose 50 systems to be conservative, as its unlikely to have more than this number in a 22 km \times 22 km rural area. Abstracting <25% of renewable freshwater represents little risk of environmental water stress according to the indicator developed for monitoring the Sustainable Development Goals³⁸. We observe in Fig. 7 that, for the majority of locations (78%), the volume pumped by the 50 PVWPS is lower than 25% of the recharged volume. However, it is important to keep in mind that Fig. 7 does not account for potentially already existing pumping systems (e.g., handpumps, diesel pumps). Additionally, the number of

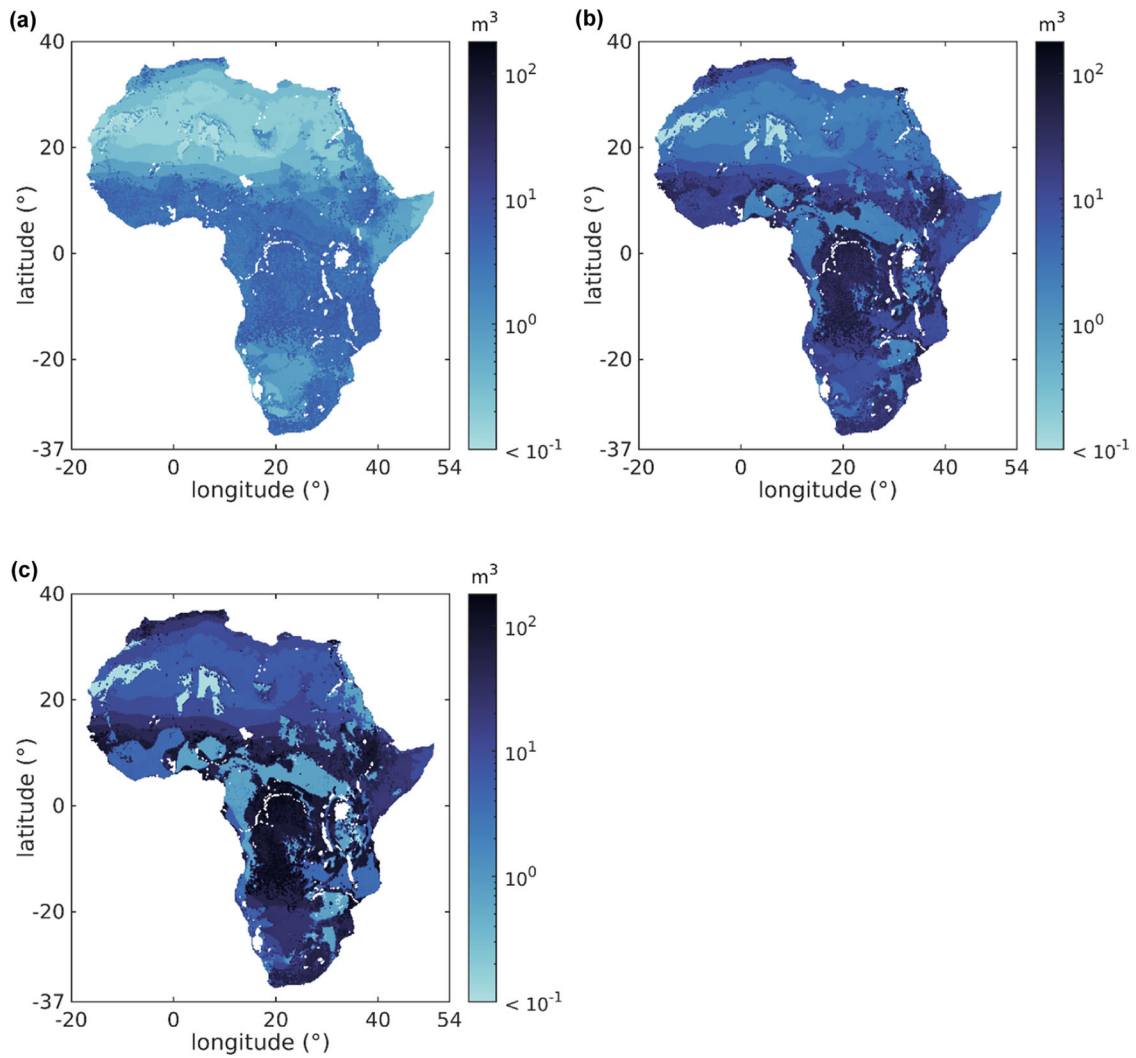


Fig. 5 Average daily pumped volume V for three PVWPS sizes. **a** $P_p = 100 W_p$, **b** $P_p = 1000 W_p$, **c** $P_p = 3000 W_p$ for 2020. The results are plotted in a blue scale.

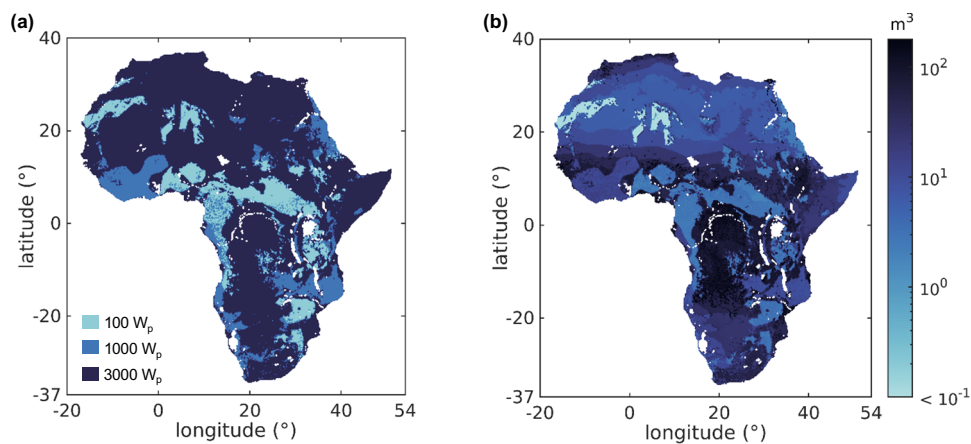


Fig. 6 Best performing PVWPS size and associated pumped volume for 2020. Size values are given in **a** and volume values in **b**. The results are plotted in a blue scale.

PVWPS considered to plot Fig. 7 (50 PVWPS) is arbitrary and the real number of systems implemented would vary from one location to another depending on the needs. Using population density³⁹ (see Fig. 8) as a proxy for demand indicates that in more

populated rural areas recharge tends to be higher, therefore, risks of over-exploitation in these areas (where PVWPS are particularly relevant) are generally low. This is consistent with recent work which showed that groundwater recharge was sufficient to

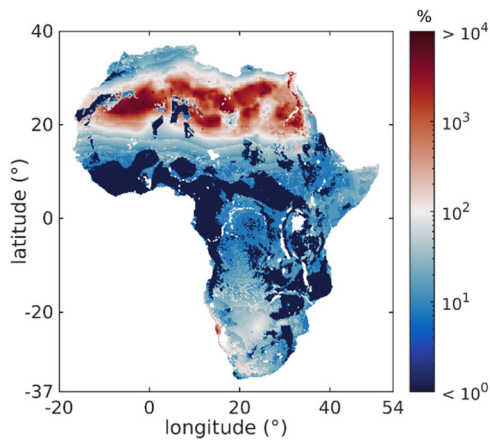


Fig. 7 Percentage of the exploitable recharge that would be extracted by 50 PVWPS of most efficient capacity. Red pixels indicate that the extraction exceeds the exploitable recharge and blue pixels that it does not.

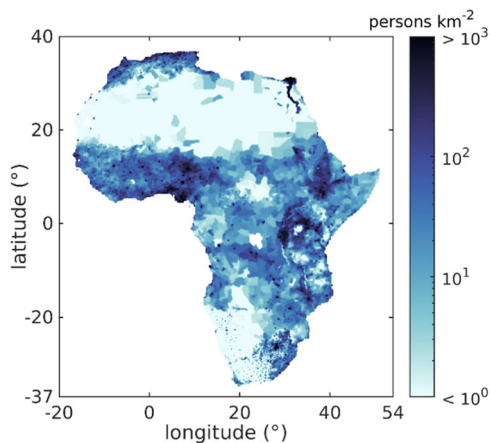


Fig. 8 Population density. The results are plotted in a blue scale. Data from ref. 39.

sustainably supply rural water supply across much of populated Africa⁴⁰.

Conclusions

We proposed a model that uses publicly and freely available groundwater and irradiance data to simulate the operation of PVWPS for any location in Africa. The model, which accounts for the different components of the PVWPS, notably simulates the evolution of the pumped flow rate and of the drawdown with a 30-min time step during a year and it considers the possible stops of the motor-pump due to excessive drawdowns. Using this model, we estimated, for all locations in Africa, the volume pumped by PVWPS of 100, 1000 and 3000 W_p . Results indicate a strong spatial variability of the pumped volume. We found that, for 27% of the positions, the largest system does not yield the highest pumped volume due to excessive drawdowns reaching the motor-pump. This is notably the case where the transmissivity and/or the saturated thickness are low. For the rest of the positions, the main driver of the pumped volume is found to be static water depth.

The first limitation of our study is the one inherent to approaches consisting of evaluating a model to a very large spatial scale (a whole continent). Both groundwater and irradiance input data have themselves been estimated and hide the specificity of the local resources. This is especially true for data regarding the

static water depth, the transmissivity and the saturated thickness where important variations may occur over a few meters. Additionally, as we have used data available for the whole Africa, the proposed model is less accurate than the model of a PVWPS for which we can access and measure all the characteristics of the site (through pumping tests for instance). Finally, the results for the pumped volume at every location do not take into consideration possible interference with neighboring pumping systems. For all these reasons, the results of this large-scale analysis should be seen as approximate that provide an overview over the continent, and as complementary to results of local and therefore more accurate analyses. In particular, as groundwater resources have a strong impact on the pumped volume and may strongly vary locally, a coordinated and detailed local investigation and monitoring of groundwater resources^{41,42} is very beneficial.

Despite these limitations, the results of this study can help identify regions or countries where PVWPS have the highest potential. In particular, they provide information on the suitability of locations in terms of pumped volume, variations of this pumped volume for extreme periods (low and high irradiance) of the year, and sustainability of the pumped volume in comparison to the recharge. They also provide insight on the most effective PVWPS size for the considered location. It may then help target investments in large-scale PV water pumping programs and identify areas where pumping potential is low and will need additional investigation to de-risk investment. This may notably be of interest to funding institutions (e.g., the World Bank, the African Development Bank) and governments. Since the model has been applied to give an initial estimate of suitability for any location in Africa (without the need to collect additional data), it can be used as a screening tool to provide a first estimate of the pumping performances of PVWPS for water sector practitioners (e.g., local companies, non-governmental organizations). Additionally, our parametric analysis provides information on the design parameters that may have the most influence on the pumped volume and which could thus be optimized first by local installers. Finally, it is possible to adapt the model to pumping systems powered by other energy sources (e.g., hand pumps, diesel pumps), by changing the “photovoltaic energy” sub-model.

Methods

PVWPS operation. The motor and the pump are built together¹⁴ and the motor-pump set is submersed in the borehole under the water⁴³. Control equipment is also installed between the PV modules and the motor-pump and/or integrated to the motor-pump set in the borehole^{14,17}. This equipment allows the motor-pump to stop and also to operate the motor-pump and the PV modules at their best operating points¹⁴. Once the water is pumped, it might then be stored in a water tank to mitigate the variability of solar resources^{14,29}. When pumping starts, a cone of depression of radius r_c is formed and there is a drawdown $H_{b,d}$ in the borehole (see Fig. 1). The higher the pumped flow rate, the higher the drawdown $H_{b,d}$ and therefore the deeper the water in the borehole H_b . If H_b reaches the position of the motor-pump H_{mp} , the motor-pump automatically switches off, therefore preventing the motor-pump from running dry⁴⁴. The motor-pump remains shut down during a period Δt_{shut} , after which it makes an attempt to restart⁴⁴.

Input data processing. We observe in Table 1 that the datasets have varying spatial resolutions. In the article, we use the spatial resolution of the irradiance map, 0.2° (~ 22 km). Indeed, this resolution is sufficient for the purposes of this article and it allows to divide computing time and memory requirements by ~ 16 in comparison to the 0.05° resolution. At this 0.2° resolution, the total area of Africa of 30 million km^2 is divided into 62,000 pixels. We apply this resolution of 0.2° to all datasets by nearest interpolation.

No exact value of the static water depth $H_{b,s}$, transmissivity T and saturated thickness H_{st} are provided for each location by the original source but only a range of variation. For instance, for -15.8° (lat) & 21.9° (lon), the saturated thickness H_{st} is comprised between 25 and 100 m. In most cases, we consider the middle of the range (e.g., 62.5 m in the example). The only two exceptions are: when $H_{b,s}$ is higher than 250 m, we consider 300 m (same for H_{st}); and, when $H_{b,s}$ is between 0 and 7 m, we consider 7 m⁴⁵. Due to the lack of available information, the input groundwater data provided in Table 1 are considered to remain constant over time.

Reference⁴⁶ provides complete irradiance data with a time step of 15 min from 2013 to 2020 across Africa. In this article, except mentioned otherwise, we use irradiance data from 2020 with a 30-min time step (by taking one point every two 15-min points), instead of all the available complete irradiance data. It divides computing time and memory requirements by ~16. Additionally, it produces reduced and acceptable deviations on the results. Indeed, for 100 randomly chosen locations, we simulated the pumped volume V , for the three considered PVWPS sizes, using (1) irradiance data from 2013 to 2020 with a 15-min time step and (2) irradiance data from 2020 with a 30-min time step. For these locations, the absolute error on volume V is systematically lower than 7.9% and the average absolute error is 2%. These results are coherent with the observed low influence of irradiance on the pumped volume in comparison to groundwater resources. Thanks to the consideration of this reduced irradiance vector, the random access memory (RAM) and the computing time required to obtain a map of final results (such as Fig. 5b) are respectively 38 Gb and 10 h (time for Intel Xeon E5-2643 3.3 GHz processors and 96 GB RAM, running on Debian 4.19.194-2), which is more reasonable.

Atmospheric sub-model. For each location, the irradiance on the plane of the PV modules G_{pv} at time t can be deduced from satellite data by^{47,48}:

$$G_{pv}(t) = G_{bn}(t)\cos(\text{AOI}(t, \theta, \alpha)) + G_{gh}(t)\kappa\frac{1 - \cos(\theta)}{2} + G_{dh}(t)\frac{1 + \cos(\theta)}{2} \quad (1)$$

where κ is the albedo of the surrounding environment, θ and α are the tilt and azimuth of the PV modules and AOI is the angle of incidence between the sun's rays and the PV modules. The albedo κ is taken equal to 0.2 because it corresponds to the albedo of cropland, which is a common environment in the rural areas considered⁴⁹. In any case, additional simulations show that the value of the albedo has a negligible effect on the pumped volume V . AOI is computed using the MATLAB toolbox PVLIB developed by the Sandia National Laboratories⁵⁰.

For each location, the azimuth α and the tilt θ of the PV modules are chosen to maximize the irradiance on the plane of the PV modules G_{pv} . The azimuth α is taken equal to⁵¹:

$$\alpha = \begin{cases} 180^\circ & \text{if } \phi > 0 \\ 0^\circ & \text{if } \phi < 0 \end{cases} \quad (2)$$

where ϕ is the latitude of the location. The tilt is taken equal to⁵¹:

$$\theta = \begin{cases} \max(10, 1.3793 + (1.2011 + (-0.014404 + 0.000080509\phi)\phi)) & \text{if } \phi > 0 \\ \min(-10, -0.41657 + (1.4216 + (0.024051 + 0.00021828\phi)\phi)) & \text{if } \phi < 0 \end{cases} \quad (3)$$

As evidenced by Eq. (3), the tilt should be higher than 10° or lower than -10°, so that the PV modules are tilted enough to be cleaned when it rains.

Photovoltaic modules sub-model. Considering that the maximum power point tracking of the PV modules is correctly performed, a simplified model to compute the power P produced by the modules is used:

$$P(t) = \frac{G_{pv}(t)}{G_0} P_p (1 - c_{pv,loss}) \quad (4)$$

where G_0 is the reference irradiance (1000 W m⁻²), P_p is the peak power of the PV modules in standard test conditions (STC) and $c_{pv,loss}$ is a coefficient that represents the losses (e.g., soiling, temperature, mismatch, wiring^{52,53}) at the level of the PV modules. For the sake of simplicity, and as we consider a generic PVWPS, we consider that $c_{pv,loss}$ is independent of the operating point of the PV modules, of the time, and of the location. We take it constant, equal to a single value (see Table 2).

Hydraulic sub-model. The total dynamic head TDH between the motor-pump and the pipe output is given by⁵⁴:

$$TDH(t) = H_b(t) + H_p(t) \quad (5)$$

where H_b is the water depth in the borehole and H_p is the additional head due to pressure losses in the pipe.

The water depth in the borehole H_b is given by (see Fig. 1)⁴²:

$$H_b(t) = H_{b,s} + H_{b,d}(t) \quad (6)$$

where $H_{b,s}$ is the static water depth and $H_{b,d}$ is the drawdown. The drawdown is composed of two parts:

$$H_{b,d}(t) = H_{b,d}^a(t) + H_{b,d}^b(t) \quad (7)$$

where $H_{b,d}^a(t)$ is the head loss due to aquifer losses and $H_{b,d}^b(t)$ is the head loss due to borehole losses.

The head loss due to aquifer losses $H_{b,d}^a(t)$ depends on the pumping flow rate Q , the aquifer transmissivity T , the borehole radius r_b , and a length parameter r_c representing the distance of water travel to replace the water pumped out. From dimensional analysis, we expect that $\frac{H_{b,d}^a(t)T}{Q(t)}$ should be a function of $\frac{r_c}{r_b}$. We thus

propose the following model for $H_{b,d}^a$, which is derived from Thiem equation⁵⁵:

$$H_{b,d}^a(t) = \frac{\ln\left(\frac{r_c}{r_b}\right)}{2\pi T} Q(t) \quad (8)$$

where r_c can be considered the effective radius of the cone of depression. This model satisfies horizontal, radial and steady Darcy flow in a uniform, homogeneous and isotropic aquifer. It captures the essential features for aquifer losses: $H_{b,d}^a(t)$ proportional to pumped flow rate and inversely proportional to transmissivity⁴⁵. Though the flow is transient, only simplified steady-state models, as the one of Eq. (8), can be applied with the available information as dynamic models would require pumping tests. Furthermore, we consider that the radius of the cone of depression r_c is comprised between 100 and 1000 m and, to correlate it to a measured quantity, that it depends linearly on the groundwater recharge R : for the lowest recharge (0 m/year), r_c is equal to 1000 m; for the highest one (0.2947 m year⁻¹), r_c is equal to 100 m; in-between, r_c is obtained linearly from the recharge ($r_c = 1000 - 3054 \cdot R$). Thus, groundwater recharge R is used to constrain the size of the cone of depression.

The head loss due to borehole losses $H_{b,d}^b(t)$ is given by⁵⁶:

$$H_{b,d}^b(t) = \beta Q(t)^2 \quad (9)$$

where β is a coefficient related to the borehole design. For the yields considered in this article, $H_{b,d}^b(t)$ usually remains lower than a few meters but, as $H_{b,d}^b(t)$ depends on the square of the pumped flow rate, it may be more important for larger abstraction capacities.

The additional head due to pipe losses H_p is given by⁵⁷:

$$H_p(t) = H_{p,ma}(t) + H_{p,mi}(t) \quad (10)$$

where $H_{p,ma}(t)$ corresponds to losses that occur along the pipe length (also called "major losses") and $H_{p,mi}(t)$ corresponds to losses at junctions such as elbows and curvatures (also called "minor losses"). $H_{p,ma}(t)$ is given by⁵⁷:

$$H_{p,ma}(t) = \frac{8f}{\pi^2 g D_p^5} L_p Q(t)^2 \quad (11)$$

where g is the gravitational acceleration (9.81 m s⁻²), D_p is the pipe diameter, L_p is the pipe length, Q is the pumped flow rate, and f is the friction coefficient between the water and the pipe. We approximate the pipe length L_p to be equal to the depth of the motor-pump H_{mp} (see Fig. 1). The expression of f depends on the value of the Reynolds number $Re = \frac{4Q}{\pi D_p w}$, where w is the water kinematic viscosity (taken equal to 1×10^{-6} m² s⁻¹)⁵⁷:

- for $Re < 3 \times 10^3$, $f = \frac{64}{Re}$,
- for $Re \geq 3 \times 10^3$, f is the solution of $\frac{1}{\sqrt{f}} = -2 \ln\left(\frac{\epsilon}{3.7D_p} + \frac{2.51}{Re\sqrt{f}}\right)$, where ϵ is the pipe roughness.

This complex formulation for f very importantly complicates the resolution of Eq. (15). To avoid this problem, we started by computing the head loss due to major losses $H_{p,ma}$ using Eq. (11), for various:

- pipe diameters D_p between 0.04 m and 0.1 m, which is an usual range for PVWPS^{58,59},
- pipe roughnesses ϵ between 0 and 1.5×10^{-4} m, which is an usual range for PVWPS^{57,58},
- flow rates Q between 0 and 5×10^{-3} m³ s⁻¹, which is an usual range for PVWPS^{29,60},
- pipe lengths L_p between 10 and 500 m, which corresponds to possible motor-pump depths.

We then fitted $H_{p,ma}$ as a function of L_p and Q , and according to²⁹:

$$H_{p,ma}(t) = \nu \cdot L_p \cdot Q^2 \quad (12)$$

where ν is a coefficient that depends on ϵ and D_p . For all the considered combinations of D_p and ϵ , we always obtained a fitting R^2 higher than 0.99. For instance, for $D_p = 0.052$ m and $\epsilon = 1.5 \times 10^{-6}$ m, we obtained $\nu = 8.9 \times 10^2$ s²m⁻⁶ with $R^2 = 0.996$. Thus, we approximate major losses with Eq. (12) and determine ν through fitting.

The head due to minor losses $H_{p,mi}(t)$ is given by:

$$H_{p,mi}(t) = K \cdot Q(t)^2 \quad \text{with} \quad K = \frac{8 \sum_{i=1}^N k_i}{\pi^2 g D_p^4} \quad (13)$$

where k_i is the coefficient associated to each junction i (values for the different junction types are provided in article⁵⁷). We neglect the dependency of k_i on the Reynolds number, as usually done⁵⁷.

Motor-pump sub-model. To determine the pumped flow rate Q , we first suppose that the motor-pump is operating, which is the case when the input power to the motor-pump P is higher than the starting power of the motor-pump $P_{mp,0}$ and when the water depth in the borehole H_b does not reach the motor-pump position

H_{mp} . When the motor-pump is operating, the pumped flow rate Q is given by^{61–63}:

$$Q(t) = \frac{P(t)\eta_{mp}}{\rho gTDH(t)} \quad (14)$$

where g is the gravitational acceleration (9.81 m s^{-2}), ρ is the water density (1000 kg m^{-3}) and η_{mp} is the motor-pump efficiency. We consider that η_{mp} is a constant for the same reasons as for the PV modules loss coefficient $c_{pv,loss}$. By integrating relations (5), (6), (7), (8), (9), (10), (12) and (13) into Eq. (14), we obtain Q by solving:

$$\left(\beta + \nu \cdot L_p + K\right)Q(t)^3 + \frac{\ln\left(\frac{r_s}{r_b}\right)}{2\pi T}Q(t)^2 + H_{b,s}Q(t) - \frac{P(t)\eta_{mp}}{\rho g} = 0 \quad (15)$$

We take the only physically feasible solution of the equation for obtaining Q .

Once Q is determined, we compute H_b thanks to Eqs. (6)–(9). If H_b is found to be higher than H_{mp} , then we in fact set Q to 0 (i.e., the motor-pump stops) for a period Δt_{shut} . After this period Δt_{shut} , the motor-pump attempts to restart.

Once Q for each 30-min time step of the year is determined, we deduce the average daily pumped volume V as following:

$$V = \frac{\int_{2020} Q(t)dt}{366} \quad (16)$$

Thus, when we use input irradiance data for 2020 with a 30-min time step, for each pixel, the average daily pumped volume V is obtained from 17568 ($=2 \times 24 \times 366$) values of pumped flow rate Q .

Data availability

The data used in this study (i.e., groundwater, irradiance and population density data) are publicly available at the following links: <https://www2.bgs.ac.uk/groundwater/international/africanGroundwater/mapsDownload.html>, <https://www2.bgs.ac.uk/nationalgeosciencedatacentre/citedData/catalogue/45d2b71c-d413-44d4-8b4b-6190527912ff.html>, <http://www.soda-pro.com/web-services/radiation/cams-radiation-service>, <https://sedac.ciesin.columbia.edu/data/set/gpw-v4-population-density-rev11> and <https://doi.org/10.5281/zenodo.7520120>. Figure 2 has associated raw data.

Code availability

The most important part of the code is available at the following link: <https://doi.org/10.5281/zenodo.7520120>. The available code allows to compute the pumped volume from the irradiance on the photovoltaic modules, using the developed model. It is a Matlab code which is commented and accompanied by a read-me file. For any questions about the code, please contact simon.meunier@centralesupelec.fr.

Received: 1 March 2022; Accepted: 1 February 2023;

Published online: 27 February 2023

References

- The Millennium Development Goals Report (UN, 2015).
- You, L. et al. What is the irrigation potential for Africa? A combined biophysical and socioeconomic approach. *Food Policy* **36**, 770–782 (2011).
- Climate change impacts and responses in small-scale irrigation systems in West Africa: Case studies in Côte d'Ivoire, the Gambia, Mali and the Niger. (FAO, 2019).
- MacDonald, A. M., Bonsor, H. C., Ó Dochartaigh, B. E. & Taylor, R. G. Quantitative maps of groundwater resources in Africa. *Environ. Res. Lett.* **7**, 024009 (2012).
- Smedley, P. L. Arsenic in rural groundwater in Ghana: part special issue: hydrogeochemical studies in sub-Saharan Africa. *J. Afr. Earth Sci.* **22**, 459–470 (1996).
- Calow, R. C., MacDonald, A. M., Nicol, A. L. & Robins, N. S. Ground water security and drought in Africa: linking availability, access, and demand. *Groundwater* **48**, 246–256 (2010).
- Taylor, R. G. et al. Ground water and climate change. *Nat. Clim. Change* **3**, 322–329 (2013).
- Progress on household drinking water, sanitation and hygiene 2000–2017: special focus on inequalities. (WHO and UNICEF, 2019).
- MacDonald, A. M., Davies, J., Calow, R. & Chilton, J. Developing Groundwater: a Guide for Rural Water Supply. (ITDG publishing, 2005).
- MacDonald, A. M. et al. Groundwater and resilience to drought in the Ethiopian highlands. *Environ. Res. Lett.* **14**, 095003 (2019).
- MacAllister, D. J., MacDonald, A. M., Kebede, S., Godfrey, S. & Calow, R. Comparative performance of rural water supplies during drought. *Nat. Commun.* **11**, 1099 (2020).
- Whaley, L. et al. Evidence, ideology, and the policy of community management in Africa. *Environ. Res. Lett.* **14**, 085013 (2019).
- Wash post-2015: proposed indicators for drinking water, sanitation and hygiene. (WHO & UNICEF, 2015).
- Chandel, S. S., Nagaraju Naik, M. & Chandel, R. Review of solar photovoltaic water pumping system technology for irrigation and community drinking water supplies. *Renew. Sustain. Energy Rev.* **49**, 1084–1099 (2015).
- Mapurunga Caracas, J. V., De Carvalho Farias, G., Moreira Teixeira, L. F. & De Souza Ribeiro, L. A. Implementation of a high-efficiency, high-lifetime, and low-cost converter for an autonomous photovoltaic water pumping system. *IEEE Trans. Ind. Appl.* **50**, 631–641 (2014).
- Burney, J., Woltering, L., Burke, M., Naylor, R. & Pasternak, D. Solar-powered drip irrigation enhances food security in the Sudano-Sahel. *Proc. Natl. Acad. Sci.* **107**, 1848–1853 (2010).
- Meunier, S. et al. Sensitivity analysis of photovoltaic pumping systems for domestic water supply. *IEEE Trans. Ind. Appl.* **56**, 6734–6743 (2020).
- Meunier, S. et al. Influence of The Temporal Resolution of The Water Consumption Profile on Photovoltaic Water Pumping Systems Modelling and Sizing. In: 7th Int. Conf. on Renewable Energy Research and Applications (ICRERA) 494–499 (2018).
- Estimating the Renewable Energy Potential in Africa (International Renewable Energy Agency, 2014): https://www.irena.org/-/media/Files/IRENA/Agency/Publication/2014/IRENA_Africa_Resource_Potential_Aug2014.pdf
- Schmitter, P., Kibret, K. S., Lefore, N. & Barron, J. Suitability mapping framework for solar photovoltaic pumps for smallholder farmers in sub-Saharan Africa. *Appl. Geogr.* **94**, 41–57 (2018).
- Gebrezgabher, S., Leh, M., Merrey, D. J., Kodua, T. T. & Schmitter, P. Solar Photovoltaic Technology for Small-scale Irrigation in Ghana: Suitability Mapping and Business Models. (International Water Management Institute, 2021).
- Salim, M. G. Selection of groundwater sites in Egypt, using geographic information systems, for desalination by solar energy in order to reduce greenhouse gases. *J. Adv. Res.* **3**, 11–19 (2012).
- Sayed, E., Riad, P., Elbeih, S., Hagra, M. & Hassan, A. A. Multi criteria analysis for groundwater management using solar energy in Moghra Oasis, Egypt. *Egypt J. Remote Sens. Space Sci.* **22**, 227–235 (2019).
- Ammar, H., Boukebous, S. E. & Benbaha, N. Photovoltaic Water Pumping System Site Suitability Analysis Using AHP GIS method In Southern Algeria. In: 4th International Conference on Renewable Energies for Developing Countries (REDEC) 1–5 (2018).
- Rubio-Aliaga, Á., García-Cascales, M. S., Sánchez-Lozano, J. M. & Molina-García, A. Multidimensional analysis of groundwater pumping for irrigation purposes: Economic, energy and environmental characterization for PV power plant integration. *Renew. Energy* **138**, 174–186 (2019).
- Yu, Y., Liu, J., Wang, Y., Xiang, C. & Zhou, J. Practicality of using solar energy for cassava irrigation in the Guangxi Autonomous Region, China. *Appl. Energy* **230**, 31–41 (2018).
- Campana, P. E. et al. Suitable and optimal locations for implementing photovoltaic water pumping systems for grassland irrigation in China. *Appl. Energy* **185**, 1879–1889 (2017).
- Xie, H., Ringler, C. & Mondal, Md. A. H. Solar or diesel: a comparison of costs for groundwater-fed irrigation in sub-saharan africa under two energy solutions. *Earth's Future* **9**, e2020EF001611 (2021).
- Meunier, S. et al. A validated model of a photovoltaic water pumping system for off-grid rural communities. *Appl. Energy* **241**, 580–591 (2019).
- Soenen, C. et al. Comparison of tank and battery storages for photovoltaic water pumping. *Energies* **14**, 2483 (2021).
- Meunier, S. et al. Modelling and optimal sizing of photovoltaic water pumping systems – Sensitivity analysis. In: 14th International Conference on Ecological Vehicles and Renewable Energies (EVER) (2019).
- Mohammed Wazed, S., Hughes, B. R., O'Connor, D. & Kaiser Calautit, J. A review of sustainable solar irrigation systems for Sub-Saharan Africa. *Renew. Sustain. Energy Rev.* **81**, 1206–1225 (2018).
- Howard, G. & Bartram, J. Domestic water quantity, service level, and health (WHO, 2003): <https://apps.who.int/iris/handle/10665/67884>.
- Cairncross, S. & Feachem, R. Environmental Health Engineering in the Tropics: Water, Sanitation and Disease Control (Routledge, 2018).
- Villholth, K. G. Groundwater irrigation for smallholders in Sub-Saharan Africa – a synthesis of current knowledge to guide sustainable outcomes. *Water Int* **38**, 369–391 (2013).
- Bakelli, Y., Arab, A. H. & Azoui, B. Optimal sizing of photovoltaic pumping system with water tank storage using LPSP concept. *Sol. Energy* **85**, 288–294 (2011).
- Kiprono, A. W. & Llarío, A. I. Solar Pumping for Water Supply. (Practical Action Publishing, 2020).
- UN-Water SDG 6 Data Portal (United Nations, 2022): <https://www.sdg6data.org/>.

39. Gridded population of the world, version 4: population density, revision 11 (Center for International Earth Science Information Network, Columbia University, 2018): <https://doi.org/10.7927/H49C6VHW>.
40. Ford, A. et al. Groundwater: the world's neglected defence against climate change (WaterAid, British Geological Survey, 2022): <https://nora.nerc.ac.uk/id/eprint/532313/>.
41. Taylor, C. J. & Alley, W. M. Ground-Water-Level Monitoring and the Importance of Long-Term Water-Level Data. (U.S. Geological Survey, 2001).
42. Vezin, T. et al. Borehole water level model for photovoltaic water pumping systems. *Appl. Energy* **258**, 114080 (2019).
43. Sontake, V. C. & Kalamkar, V. R. Solar photovoltaic water pumping system - a comprehensive review. *Renew. Sustain. Energy Rev.* **59**, 1038–1067 (2016).
44. Campana, P. E. et al. Economic optimization of photovoltaic water pumping systems for irrigation. *Energy Convers. Manag.* **95**, 32–41 (2015).
45. Bonsor, H. C. & MacDonald, A. M. An initial estimate of depth to groundwater across Africa (British Geological Survey, 2011): <http://nora.nerc.ac.uk/id/eprint/17907>
46. Copernicus Atmosphere Monitoring Service (CAMS) (European Commission, 2021): <http://www.soda-pro.com/web-services/radiation/cams-radiation-service>.
47. Fraas, L. & Partain, L. Solar Cells and Their Applications - 2nd Edn. (Wiley, 2010).
48. Meunier, S. et al. Effect of irradiance data on the optimal sizing of photovoltaic water pumping systems. In: 2019 IEEE 46th Photovoltaic Specialists Conference (PVSC) 0653–0658 (2019).
49. Carrer, D., Pique, G., Ferlicoq, M., Ceamanos, X. & Ceschia, E. What is the potential of cropland albedo management in the fight against global warming? A case study based on the use of cover crops. *Environ. Res. Lett.* **13**, 044030 (2018).
50. PVLIB Toolbox (Sandia National Laboratories, 2018): https://pypmc.sandia.gov/applications/pv_lib-toolbox/.
51. Jacobson, M. Z. & Jadhav, V. World estimates of PV optimal tilt angles and ratios of sunlight incident upon tilted and tracked PV panels relative to horizontal panels. *Sol. Energy* **169**, 55–66 (2018).
52. Gong, A. Understanding PV system losses (Aurora Solar, 2018): <https://www.aurorasolar.com/blog/understanding-pv-system-losses-part-1/>.
53. Lee, J. T. & Callaway, D. S. The cost of reliability in decentralized solar power systems in sub-Saharan Africa. *Nat. Energy* **3**, 960–968 (2018).
54. Campana, P. E., Li, H. & Yan, J. Dynamic modelling of a PV pumping system with special consideration on water demand. *Appl. Energy* **112**, 635–645 (2013).
55. Thiem A. Die Ergiebigkeit artesischer Bohrlöcher, Schachtbrunnen und Filtergalerien [The yield of artesian boreholes, shaft wells and filter galleries]. *J. Gasbeleucht Wasserversorg* **13**, 450–467 (1870).
56. Bierschenk, W. H. Determining well efficiency by multiple step-drawdown tests. International Association of Scientific Hydrology (1963).
57. Munson, B. R., Young, D. F. & Okiishi, T. H. Fundamentals of Fluid Mechanics. (Wiley, 2006).
58. Caton, P. Design of rural photovoltaic water pumping systems and the potential of manual array tracking for a West-African village. *Sol. Energy* **103**, 288–302 (2014).
59. Muhsen, D. H., Ghazali, A. B. & Khatib, T. Multiobjective differential evolution algorithm-based sizing of a standalone photovoltaic water pumping system. *Energy Convers. Manag.* **118**, 32–43 (2016).
60. SQFlex - Renewable-energy-based water supply systems (Grundfos, 2020)
61. Boutelhig, A., Bakelli, Y., Hadj Mohammed, I. & Hadj Arab, A. Performances study of different PV powered DC pump configurations for an optimum energy rating at different heads under the outdoor conditions of a desert area. *Energy* **39**, 33–39 (2012).
62. Acakpovi, A., Xavier, F. F. & Awuah-Baffour, R. Analytical method of sizing photovoltaic water pumping system. In: 4th International Conference on Adaptive Science & Technology (ICAST), 65–69 (2012).
63. Protogeropoulos, C. & Pearce, S. Laboratory evaluation and system sizing charts for a 'second generation' direct PV-powered, low cost submersible solar pump. *Sol. Energy* **68**, 453–474 (2000).
64. MacDonald, A. M. et al. Mapping groundwater recharge in Africa from ground observations and implications for water security. *Environ. Res. Lett.* **16**, 034012 (2021).
65. MacDonald, A. M., Bonsor, H. C., Ó Dochartaigh, B. E. & Taylor, R. G. Digital groundwater maps of Africa (2012): <https://www2.bgs.ac.uk/groundwater/international/africanGroundwater/mapsDownload.html>.
66. MacDonald, A. M. et al. Groundwater recharge in Africa from ground based measurements (2020): <https://www2.bgs.ac.uk/nationalgeosciencedatacentre/citedData/catalogue/45d2b71c-d413-44d4-8b4b-6190527912ff.html>.
67. Meunier, S., Kitanidis, P. K., Cordier, A. & MacDonald, A. M., Code associated with 'Aquifer conditions, not irradiance determine the potential of photovoltaic energy for groundwater pumping across Africa' (Zenodo, 2023): <https://doi.org/10.5281/zenodo.7520120>.
68. SQFlex - submersible groundwater pumps (Grundfos, 2021): <https://product-selection.grundfos.com/products/sqflex?tab=models>.
69. Meunier, S. Optimal design of photovoltaic water pumping systems for rural communities – a technical, economic and social approach. PhD thesis, Université Paris-Saclay (2019).
70. Allouhi, A. et al. PV water pumping systems for domestic uses in remote areas: sizing process, simulation and economic evaluation. *Renew. Energy* **132**, 798–812 (2019).
71. Bäverman, G. & Tavooosi, E. Evaluation of a solar powered water pumping system in Mutomo, Kenya: Comparison between a submersible induction motor and a PMSM system. MSc thesis, Uppsala Universitet (2019).
72. Smith, C. C. Rural boreholes and wells in Africa - economics of construction in hard rock terrain. *J. Am. Water Works Assoc.* **95**, 100–111 (2003).

Acknowledgements

The authors thank Loïc Quéval for his advice and comments. The authors also thank the reviewers for their comments.

Author contributions

S.M. conceived the original idea, developed the model, curated data, developed the code and wrote the manuscript draft. P.K.K. conceived the original idea and developed the model. A.C. curated data and developed the code. A.M.M. developed the model and curated data. All authors developed the analysis and conclusions and reviewed the manuscript.

Competing interests

The authors declare no competing interests.

Additional information

Supplementary information The online version contains supplementary material available at <https://doi.org/10.1038/s43247-023-00695-8>.

Correspondence and requests for materials should be addressed to Simon Meunier.

Peer review information *Communications Earth & Environment* thanks Shyam Chandel, Pietro Campana, Jennifer Burney and the other, anonymous, reviewer(s) for their contribution to the peer review of this work. Primary Handling Editors: Rahim Barzegar and Joe Aslin.

Reprints and permission information is available at <http://www.nature.com/reprints>

Publisher's note Springer Nature remains neutral with regard to jurisdictional claims in published maps and institutional affiliations.



Open Access This article is licensed under a Creative Commons Attribution 4.0 International License, which permits use, sharing, adaptation, distribution and reproduction in any medium or format, as long as you give appropriate credit to the original author(s) and the source, provide a link to the Creative Commons license, and indicate if changes were made. The images or other third party material in this article are included in the article's Creative Commons license, unless indicated otherwise in a credit line to the material. If material is not included in the article's Creative Commons license and your intended use is not permitted by statutory regulation or exceeds the permitted use, you will need to obtain permission directly from the copyright holder. To view a copy of this license, visit <http://creativecommons.org/licenses/by/4.0/>.

© The Author(s) 2023